Pt Skin on Structurally Ordered PdFe/C Intermetallic Nanoparticles for Efficient Hydrogen Oxidation Reaction in Alkaline Media

Weiping Xiao,[a,1] Wen Lei,[a,1] Jie Wang,[c] Guoying Gao,[d] Tonghui Zhao,[a] Macro A.L. Cordeiro,[b] Ruoqian Lin,[b] Mingxing Gong,[a] Xuyun Guo, [c] Eli Stavitski,[e] Huolin L. Xin,[b] Ye Zhu,[c] and Deli Wang,[a,*]

a Key laboratory of Material Chemistry for Energy Conversion and Storage (Huazhong University of Science and Technology), Ministry of Education, Hubei Key Laboratory of Material Chemistry and Service Failure, School of Chemistry and Chemical Engineering, Huazhong University of Science and Technology, Wuhan, 430074, P.R. China. E-mail: wangdl81125@hust.edu.cn

b Center for Functional Nanomaterials, Brookhaven National Laboratory, Upton, NY, USA

c Department of Applied Physics, The Hong Kong Polytechnic University, Hung Horn, Kowloon, Hong Kong

d School of Physics, Huazhong University of Science and Technology, Wuhan 430074, China

e National Synchrotron Light Source II (NSLS-II), Brookhaven National Laboratory, Upton, NY, USA

Supporting Information Placeholder

ABSTRACT: Tuning the hydrogen adsorption energy (E_H) by precisely controlling the surface electronic structure of Pt is essential to enhance hydrogen oxidation reaction (HOR) performance in alkaline media. This could be achieved by forming Pt skin on PdFe/C nanoparticles with structurally ordered intermetallic (O-PdFe@Pt/C) or disordered alloy (D-PdFe@Pt/C). The HOR activity on O-PdFe@Pt/C exhibits an exchange current density of 1.18 A mg_{Pt}^{-1}, which is 3.3 and 7.2 times higher than that on D-PdFe@Pt/C (0.36 A mg_{Pt}^{-1}) and Pt/C (0.164 A mg_{Pt}^{-1}), respectively. The excellent electrocatalytic HOR performance on O-PdFe@Pt/C could be ascribed to the attenuation of the E_H on Pt shell induced by the structurally ordered PdFe core, where the E_H on O-PdFe@Pt surface is 0.18 eV smaller than Pt according to DFT calculations.

The anion exchange membrane fuel cell (AEMFC) has aroused increasing research interests since a wide range of abundant and inexpensive catalysts can replace Pt-group metals to catalyzing oxygen reduction reaction (ORR) and significantly reduce the cost of fuel cell.[1-9] However, the hydrogen oxidation reaction (HOR) kinetic on Pt-group catalysts (Pt, Pd, Ir) in alkaline electrolyte is much sluggish with the exchange current density (i_0) of about 100 times slower than in acidic electrolyte.[10-13] At the current stage of technology, Pt is reported to be the most active HOR catalyst in alkaline electrolyte and has great potential to acquire commercially viable power densities.[14] The main obstacle lies in the large overpotential, high cost and poor stability of Pt. Wang and coworkers have indicated that the peak power density on PtRu alloy is twice higher than Pt for the AEMFC, suggesting the incorporation of Ru can affect electronic structure of Pt and weak the Pt-H_{ad} interaction, which is beneficial to the HOR in base.[15] The research on the correlation between hydrogen binding energy (HBE) and pH indicate that the HBE of each metal increases linearly with pH value, suggesting the slower HOR kinetics in base could be ascribed to the higher HBE.[12,14,16] Moreover, alloying a portion of the costly Fe, Co, Ru, Cu, Au with Pt can exhibit favorable HOR performance due to the synergistic ligand and strain effects.[17] Recent research indicates that the HOR kinetic is restricted by the Volmer step ($H_{ad}+OH^- \leftrightarrow H_2O+e^-+*$) in alkaline media, thus, it is reasonable to believe that the weaker hydrogen adsorption may be conductive to the significant enhancement of HOR performance.[13,15,18]

To maximize the utilization efficiency of Pt and reduce the cost of the catalyst, core-shell structure nanoparticles with one to two layers of Pt on the surface of less-precious Pd-based alloy have aroused much attention. On the one hand, the dissolution rates of Pd in 1 M KOH are significantly lower than that measured in acidic electrolytes.[19] In contrast, Pt/C catalyst is demonstrated to suffer severe degradation in base electrolyte.[20] Hence, forming a core-shell structure can enhance the efficiency of Pt and the durability of the electrocatalysts. On the other hand, structurally ordered Pd-based intermetallic nanoparticles, relative to disordered alloy phase, have stronger electronic interaction between Pd and smaller *3d*-transition metals, which may cause the attenuation of the hydrogen adsorption and then enhance the HOR performance.[21-27] The intense electronic effect could further reduce the electronic density of Pt by forming the core-shell structure catalyst with structurally ordered Pd-based core and Pt shell.[28,29] The change of the electronic structure on Pt could cause down shift of *d*-band center and then weaken the hydrogen adsorption energy, which could contribute to higher HOR activity.[16,30-32]

Herein, by precise regulation the annealing temperature, the surface electronic structure of Pd can be controlled by the structure transformation from disordered PdFe/C alloys (D-PdFe/C) to structurally ordered PdFe/C intermetallic nanoparticles (O-PdFe/C). The different electronic structure between D-PdFe/C and

O-PdFe/C could result in the difference of electronic effect of Pt by forming Pt skin on the surfaces of PdFe/C nanoparticles (O-PdFe@Pt/C and D-PdFe@Pt/C). Compared with Pt/C, the higher HOR kinetics on O-PdFe@Pt/C can be attributed to the weakening of hydrogen adsorption on Pt shell caused by the tightly packed ordered PdFe structure. Most importantly, the structurally ordered Pd-based core can improve the utilization of Pt and render the core-shell structure catalyst prohibitively durable owing to the electronic effect and strain effect between Pd, Fe and Pt.

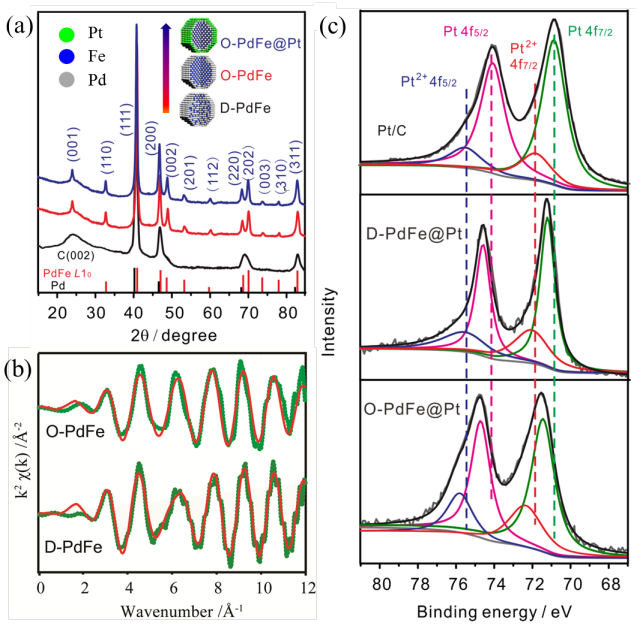

Figure 1. (a) XRD of D-PdFe/C, O-PdFe/C and O-PdFe@Pt/C nanoparticles. The vertical red and black lines are corresponding to $L1_0$-ordered PdFe (PDF card # 00-002-1440) and *fcc*-Pd (PDF card # 01-089-4897), respectively. (b) k^2-weighted extended X-ray absorption fine structure (EXAFS) region (green dots) together with the best-fit simulation of the data (red line) with the parameters given in the Table S1. (c) The fine spectra of Pt 4f on Pt/C, D-PdFe@Pt/C and O-PdFe@Pt/C catalysts.

PdFe/C bimetallic nanoparticles with disordered and structurally ordered intermetallic structure were prepared by an impregnation reduction process modified by our earlier work.[33] Post-annealing time and temperature were adjusted to incorporating Fe atom into the Pd lattice, where longer time and higher temperature are conducive to the formation of ordered structure. The structural difference between disordered (D-PdFe/C) and ordered (O-PdFe/C) phase could be certificated from XRD (Figure 1a). The four peaks on D-PdFe/C nanoparticles are the characteristic of disordered face centered cubic (*fcc*) Pd corresponding to PDF card # 01-089-4897, further proved the formation of alloying phase, as the peaks position shifted to high angles relative to Pd/C (Figure S1). The appearance of super-lattice diffraction peaks of (001), (110), and (002), absent in D-PdFe/C, became the direct evidence in forming the ordered PdFe/C phase, indicating the crystal structure was transformed from disordered *fcc* to $L1_0$ ordered structure. The lattice parameters, calculated from Debye-Scherrer equation, indicated that the lattice of Pd on O-PdFe/C was further shrunk than D-PdFe/C (Table S2). The intense electronic effect could change the electronic density of Pt by forming a Pt shell on O-PdFe/C (O-PdFe@Pt/C). Compared with O-PdFe/C, the peak position of (111) crystal surface on O-PdFe@Pt/C nanocatalyst exhibits slightly negative shift, indicating the Pt is successfully modified on the O-PdFe/C surface and gives rise to the lattice expansion of Pd.

X-ray absorption spectra at the Pd K-edge were conducted to analysis the structure of the prepared nanoparticles. The XANES spectra of both O-PdFe/C and D-PdFe/C, shown in the Figure S2, exhibit two-peak patterns and are consistent with the metallic Pd as described in previous study.[34] The intensity of Pd in O-PdFe was slightly increased relative to that in D-PdFe, suggesting the higher density of unoccupied d states and lower electronic density of Pd on the O-PdFe/C. The difference between the two samples manifests themselves in the EXAFS region (Figure 1b). Simulations of the EXAFS data with best fit-parameters given in Table S1 using two Pd-Pd and Pd-Fe scattering paths yields the ratio of the Pd-Fe and Pd-Pd coordination numbers $n_{Pd\text{-}Fe} / n_{Pd\text{-}Pd} = 8/4$, which is expected from the well-ordered lattice. The different $n_{Pd\text{-}Fe} / n_{Pd\text{-}Pd}$ ratio for the D-PdFe/C (1.4) value indicates the segregation of the two metals.

The structure difference of D-PdFe/C and O-PdFe/C could result in the difference of the *d*-band center and electron density of Pt when forming Pt shell on the surfaces. In order to determine the surface components and electronic state of the nanoparticles, XPS spectra is conducted and analyzed. Figure 1c shows the behavior of the Pt 4f peaks of Pt/C, D-PdFe@Pt/C, and O-PdFe@Pt/C catalysts, respectively. For each of the samples, there are two characteristic peaks corresponding to Pt $4f_{5/2}$ (the higher energy peak) and the Pt $4f_{7/2}$ (the lower energy peak), respectively. The higher strength peaks on Pt/C nanoparticles at 74.06 and 70.80 eV are respond to Pt $4f_{5/2}$ and Pt $4f_{7/2}$, respectively. The weaker strength peaks at 75.50 and 71.82 eV could be considered as oxidized Pt (Table S3).[17] Compared with Pt/C, the peak position of D-PdFe@Pt/C and O-PdFe@Pt/C catalysts shifted to higher binding energies, indicating the reduction of Pt *d*-band center and then leads to the weaker adsorption of hydrogen (Table S3). It is generally accepted that the HOR reaction in alkaline media is limited to the Volmer step (H_{ad}+OH-↔H_2O+e-+*).[15] Therefore, it is reasonable to consider that core-shell structure catalysts should exhibit better HOR kinetics relative to Pt/C for the weakening of hydrogen adsorption. Furthermore, the higher binding energies on O-PdFe@Pt/C nanocatalysts suggest the stronger electron effect of Pt relative to D-PdFe@Pt/C and may lead to better HOR kinetics.

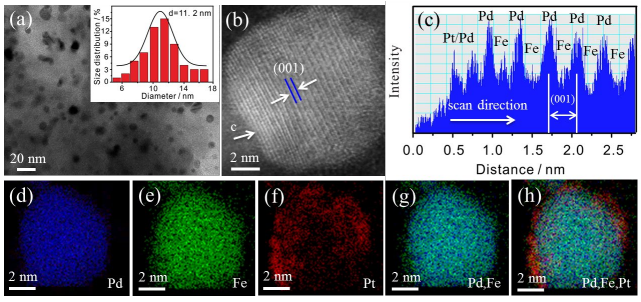

Figure 2. (a) The overview TEM image of O-PdFe@Pt/C nanoparticles. The inset shows the particle size distribution. (b) HAADF-STEM image of one O-PdFe@Pt/C nanoparticle. The inset shows superlattice crystal surface of (001) axis. (c) HAADF-STEM image of one O-PdFe nanoparticle with the scan direction from the shell to the core along the white arrow in b. EDX-mapping of Pd (d), Fe (e), Pt (f), overlapping of Pd and Fe (g), overlapping of Pd, Fe and Pt (h) for one O-PdFe@Pt/C nanoparticle.

The overview TEM image of O-PdFe@Pt/C nanoparticles in Figure 2a shows that the particles are uniformly dispersed on carbon support with main particle size of 11.2 nm. To investigate the ordered structure and the elemental distribution characteristics of O-PdFe@Pt/C from the atomic level, aberration-corrected HAADF-STEM images of one nanoparticle in (001) orientation are shown in Figure 2b. The crystalline interplanar spacing is

measured to be 0.373 nm, corresponding well to the (001) plane of the ordered PdFe $L1_0$ structure, which indicates the ordered structure is well maintained after Pt decoration. Along the scanning direction in Figure 2b, the intensity fluctuation is observed since the Pd and Pt atoms are much brighter than that of Fe atoms. Compared with the alternating intensities at the O-PdFe core, there are only brighter intensities of Pd or Pt atoms near the surface, indicating one to two layers of Pt shell on the surface of ordered core (Figure 2c). Distinguishing elements by their intensity contrast, the crystalline interplanar spacing are measured to be 0.373 nm and correspond well to the (001) plane of the ordered PdFe $L1_0$ structure, which is consistent to the ideal atomic arrangement (inset in Figure S2). The Pt shell is further proved from the EDX mappings of Pt, Pd, Fe (Figure 2d-h) and the amount of Pt is analyzed by ICP-AES, which show that the atomic ratio of Pd and Pt is almost 9.6:1, close to the theoretical proportion of 10:1 (Table S4).

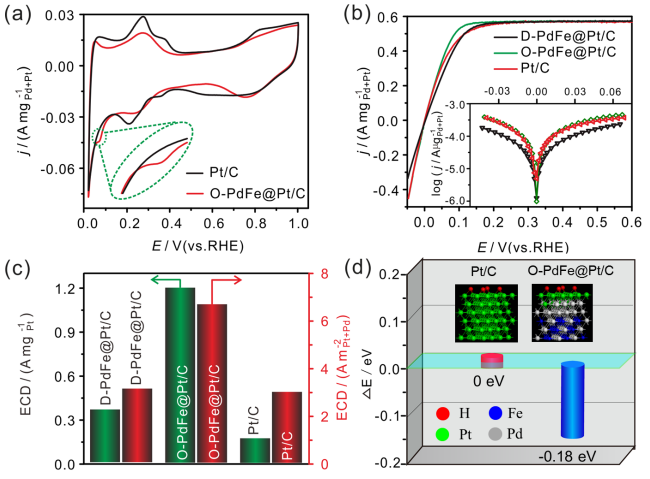

Figure 3. (a) CV curves of Pt/C and O-PdFe@Pt/C catalysts in 0.1 M KOH. (b) HOR polarization curves of Pt/C, D-PdFe@Pt/C and O-PdFe@Pt/C catalysts. The inset shows the corresponding HER/HOR Tafel plots. (c) The i_0 (obtained from Tafel plots) normalized to the mass and ECSA, respectively. (d) DFT-calculated hydrogen adsorption energy (ΔE) on O-PdFe@Pt/C surfaces relative to Pt/C.

Figure 3a compares the CV curves of O-PdFe@Pt/C and Pt/C nanoparticles. There is a positive shift on reduction onset potential of oxygen species on O-PdFe@Pt/C electrode relative to Pt/C since the smaller core atoms (Pd, Fe) changed the electronic density of Pt shell and lead to a weak adsorption of oxygen species on Pt surface. For Pt/C catalyst, the Pd-H desorption (H_{upd}) peaks at 0.38 V and 0.275 V are corresponding to the (100) and (110) crystal surface of Pt, respectively. In contrast, only one broad peak at 0.29 V appears on D-PdFe@Pt/C and O-PdFe@Pt/C catalyst, indicating the modified loading of Pt is relatively low and not exhibit the unique 110 and 100 facets (Figure 3a, S3). In the lower potential region (0.04 V~0.1 V), there are a pair of weak H_{upd} peaks on D-PdFe@Pt/C and O-PdFe@Pt/C catalyst, not present on Pt/C, which could be attributed to the electronic and geometry effect caused by the PdFe core. This suggests that H_{upd} processes on core-shell structure is significantly accelerated relative to Pt/C.[35] In previous studies, the weaker H_{upd} usually means the attenuation of hydrogen adsorption energy and the enhancement of HOR performance.[12,36] The electrochemically active areas (ECSAs) are calculated from the CO-stripping voltammetry curves (Figure S4, S5). The ECSAs of D-PdFe/C and O-PdFe/C catalysts are enhanced after Pt decoration, indicating the exposure of more active sites and better performance on D-PdFe@Pt/C and O-PdFe@Pt/C nanoparticles.

Figure 3b shows the polarization curves of HOR on Pt/C, D-PdFe@Pt/C and O-PdFe@Pt/C catalysts. The half-wave potential is at 38 mV on O-PdFe@Pt/C, almost the same as that on Pt/C (40 mV), which is significantly enhanced relative to Pd/C (245 mV), D-PdFe/C (207 mV), O-PdFe/C (192 mV) and D-PdFe@Pt/C (53 mV) catalysts (Figure S6 and Table S5). Compared with D-PdFe@Pt/C, the dramatically enhanced HOR kinetics on O-PdFe@Pt/C electrode could be ascribed to the contracted lattice of Pt caused by the structurally ordered intermetallic PdFe core, corresponding to the stronger electron effect of Pt as analyzed in XPS result. The above analysis shows that the formation of intermetallic PdFe core and Pt shell could be conducive to the enhancement of HOR activity.

The relationship between current density and over-potential under electrochemical polarization following the Butler-Volmer equation:

$$i = i_o[\exp\left(\frac{\alpha nF}{RT}\eta\right) - \exp\left(-\frac{(1-\alpha)nF}{RT}\eta\right)] \qquad (1)$$

Here, i is the measured current density; i_0 is the exchange current density; η is the overpotential; α is the transfer coefficient; R is the gas constant (8.314 J·mol^{-1} K^{-1}), T is the Kelvin temperature (298 K), F is the Faraday's constant (96,485 C mol^{-1}). If the electrode under strong polarization condition, the equation (1) can be neglected to $i = i_o \exp\left(\frac{\alpha nF}{RT}\eta\right)$, namely the Tafel equation: $\eta = a + b\log i$. The inset of Figure 3b and Figure S7 show the Tafel curves of Pd/C, D-PdFe/C, O-PdFe/C Pt/C, D-PdFe@Pt/C and O-PdFe@Pt/C catalysts. The Butler-Volmer fitting i_0 were obtained from the Tafel equation. The i_0 normalized to the ECSA on O-PdFe@Pt/C exhibited 6.65 A m_{Pt+Pd}^{-2}, which is 2.15 and 2.23 times higher than that on D-PdFe@Pt/C (3.09 A m_{Pt+Pd}^{-2}) and Pt/C (2.98 A m_{Pt}^{-2}), respectively. The i_0 normalized to the mass of Pt on O-PdFe@Pt/C exhibited 1.18 A mg_{Pt}^{-1}, which is 3.3 and 7.2 times higher than that on D-PdFe@Pt/C (0.36 A mg_{Pt}^{-1}) and Pt/C (0.164 A mg_{Pt}^{-1}), respectively (Figure 3c and Table S6).

If the electrode under micropolarization condition, the equations (1) can be neglected to: $i = i_o \frac{nF}{RT}\eta$. The i_0 can be obtained from the slope of liner polarization curves from -5 mV to 5 mV (Figure S8). The i_0 normalized to the ECSA and the mass of Pt on O-PdFe@Pt/C exhibited 7.76 A m^{-2} and 1.15 A mg_{Pt}^{-1}, much higher than that on D-PdFe@Pt/C (6.67 A m_{Pt+Pd}^{-2}, 0.78 A mg_{Pt}^{-1}) and Pt/C (3.67 A m_{Pt}^{-2}, 0.21 A mg_{Pt}^{-1}) (Figure S9 and Table S7). The HOR activity on O-PdFe@Pt/C is much better than the reported materials in terms of i_0 (Table S8).

Compared with Pd/C, O-PdFe/C and D-PdFe/C catalysts, Pt/C, D-PdFe@Pt/C and O-PdFe@Pt/C exhibit higher exchange current density and better HOR activity since the H adsorption/desorption on Pt/C are more reversible relative to Pd/C (Table S6, S7). Forming O-PdFe@Pt/C and D-PdFe@Pt/C greatly improve the utilization of Pt without the compensation of performance. Furthermore, the excellent HOR activity on O-PdFe@Pt/C relative to D-PdFe@Pt/C could be ascribed to the weaker hydrogen adsorption derived from contracted Pt lattice caused by the ordered PdFe core, implying that the electronic structure of Pt has significant impacts on the HOR activities. This is corresponding to the XPS result that the reduction of Pt electron density on O-PdFe@Pt/C may lead to a weaker adsorption of hydrogen and higher HOR kinetics. To better explore the relationship between HOR performance and hydrogen adsorption energies (E_H), DFT calculations are conducted. In convenience, the E_H on Pt/C crystal plane is treated as the reference and ΔE is defined relative to E_H on Pt/C surface. It is clear that the ΔE on O-PdFe@Pt surface is 0.18 eV smaller than the bulk Pt (Figure 3d), which could be attributed to the change of electronic effect on Pt surface (Figure 1c). The higher binding energies on O-PdFe@Pt/C relative to D-

PdFe@Pt/C reflect the stronger electron effect of Pt and then exhibited weaker E_H. The above analysis provide a clear indication that the excellent HOR performance on O-PdFe@Pt/C could be ascribed to the lower E_H induced by electronic effect between ordered PdFe core and Pt shell. Hence, the core-shell structure O-PdFe@Pt/C catalyst exhibits the similar HOR performance to Pt/C and greatly improves the utilization of Pt. Having excellent performance, the O-PdFe@Pt/C nanoparticles are promising as HOR catalysts for alkaline fuel cells.

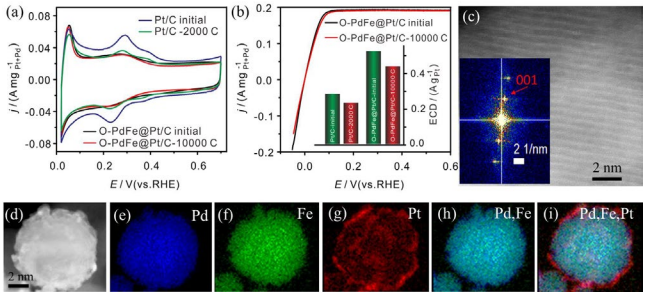

Figure 4. (a) CV curves of Pt/C and O-PdFe@Pt/C catalysts before and after durability test (Pt/C-2,000 cycles, O-PdFe@Pt/C-10,000 cycles). (b) LSV curves of O-PdFe@Pt/C catalyst before and after 10,000 cycles durability test. The inset shows the i_0 normalized to the mass of Pt. (c) HAADF-STEM image of one O-PdFe@Pt nanoparticle after durability test, the inset shows the diffractogram patterns from (001) zone axis. (d) STEM image of one O-PdFe@Pt/C nanoparticle after durability test. EDS-mapping of Pd (e), Fe (f), Pt (g), overlapping of Pd and Fe (h), overlapping of Pd, Fe and Pt (i) for one O-PdFe@Pt/C nanoparticle.

The stability of O-PdFe@Pt/C and Pt/C catalysts were measured by potential cycling between 0.02 and 1.0 V in N_2-saturated 0.1 M KOH solution at a scanning rate of 100 mV s^{-1}. The CV curves of O-PdFe@Pt/C exhibit almost no change after 10,000 cycles while there is a fast decay on Pt/C for only 2,000 cycles (Figure 4a). Figure 4b and Figure S10 show the HOR polarization curves of O-PdFe@Pt/C and Pt/C catalyst before and after durability test, respectively. The half-wave potential on O-PdFe@Pt/C catalyst shifts negatively of 3 mV for 10,000 cycles, which is slightly lower than that on Pt/C with 8 mV for only 2,000 cycles. The comparison of linear polarization plots on Pt/C and O-PdFe@Pt/C catalyst before and after durability test are shown in Figure S11. The exchange current density obtained from liner polarization curves on O-PdFe@Pt/C attenuated about 16.2% after 10,000 cycles, much lower than that of Pt/C (18.6%) for 2,000 cycles (inset in Figure 4b). Moreover, the exchange current density obtained from Tafel curves on O-PdFe@Pt/C decreased about 16.8% after 10,000 cycles, which is much lower than that of the Pt/C (21.3%) electrode for only 2,000 cycles, indicating more stable of O-PdFe@Pt/C relative to Pt/C (Figure S12, S13 and Table S9). To better investigate the stabilization effect, HAADF-STEM images of O-PdFe@Pt/C catalyst after durability test were conducted. The super-lattice (001) face, shown in Figure 4c, was still existence, suggesting the ordered structure was maintained after durable test. Furthermore, the presence of Pt shell was further proved from the elemental maps of Pt, Pd and Pt, Pd, Fe (Figure 4d-i). Hence, the superior durability on O-PdFe@Pt/C can be ascribed to the stable nature of Pd in alkaline medium and the electronic effect of the O-PdFe core to Pt shell. The stabilization effect could be contributed to the much larger size avoiding the aggregation of particles on account of the Oswald ripening effect.

In summary, precisely control the arrangement of atoms at the individual nanoparticle level could be achieved by the structural transformation from disordered PdFe/C alloys to structurally ordered PdFe intermetallics. The structure difference could arouse the change of surface electronic structure of Pt after forming a Pt skin on PdFe/C nanoparticles. The O-PdFe@Pt/C exhibits superior HOR activity, comparable to Pt/C, relative to D-PdFe@Pt/C. The analyses down to the atomic level demonstrate that the excellent activity on O-PdFe@Pt/C could be ascribed to compressively strained atomic layer of Pt induced by the ordered PdFe core, resulting in the downward shift of *d*-band center and the weaker adsorption of hydrogen at the surface of Pt. More importantly, the stable nature of Pd and intermetallic structure make the O-PdFe@Pt/C nanoparticles extremely stable on account of the electronic effects between the structurally ordered PdFe core and Pt shell. This work provides new insights for the future optimization of the HOR electrocatalysts.

ASSOCIATED CONTENT

Supporting Information

The Supporting Information is available free of charge on the ACS Publications website.

AUTHOR INFORMATION

The manuscript was written through contributions of all authors. All authors have given approval to the final version of the manuscript. W. Xiao and W. Lei contributed equally.

Corresponding Author

wangdl81125@hust.edu.cn;

ACKNOWLEDGMENT

This work was supported by the National Natural Science Foundation (21573083), 1000 Young Talent (to Deli Wang), and the Innovation Research Funds of Huazhong University of Science and Technology (2017KFYXJJ164). We thank Analytical and Testing Center of Huazhong University of Science & Technology for allowing us to use its facilities for XRD, XPS measurements. STEM-EDS mapping was carried out at the Department of applied physics, The Hong Kong Polytechnic University, which are supported by the Hong Kong Research Grants Council through the Early Career Scheme (Project No. 25301617) and the Hong Kong Polytechnic University grant (Project No. 1-ZE6G). J.W. and Y.Z. thanks Dr. Lu Wei for optimizing the JEOL JEM-2100F microscope. High-resolution STEM imaging made use of the Center for Functional Nanomaterials, Brookhaven National Laboratory, which is supported by the U.S. Department of Energy, Office of Basic Energy Sciences, under Contract No. DE-SC0012704. XAS used 8-ID (ISS) beamline of the National Synchrotron Light Source, a U.S. Department of Energy (DOE) Office of Science User Facility operated for the DOE Office of Science by Brookhaven National Laboratory under Contract No. DE-AC02-98CH10886.

REFERENCES

(1) Wang, Y. J.; Qiao, J.; Baker, R.; Zhang, J. *Chem. Soc. Rev.* **2013**, *42*, 5768.
(2) Li, C.; Han, X.; Cheng, F.; Hu, Y.; Chen, C.; Chen, J. *Nat. Commun.* **2015**, *6*, 7345.
(3) Varcoe, J. R.; Atanassov, P.; Dekel, D. R.; Herring, A. M.; Hickner, M. A.; Kohl, P. A.; Kucernak, A. R.; Mustain, W. E.; Nijmeijer, K.; Scott, K. *Energy & Environ. Sci.* **2014**, *7*, 3135.
(4) Zhuang, Z.; Giles, S. A.; Zheng, J.; Jenness, G. R.; Caratzoulas, S.; Vlachos, D. G.; Yan, Y. *Nat. Commun.* **2016**, *7*.
(5) Setzler, B. P.; Zhuang, Z.; Wittkopf, J. A.; Yan, Y. *Nat. Nanotech.* **2016**, *11*, 1020.
(6) Chung, H. T.; Won, J. H.; Zelenay, P. *Nat. Commun.* **2013**, *4*, 1922.

(7) Sa, Y. J.; Park, C.; Jeong, H. Y.; Park, S. H.; Lee, Z.; Kim, K. T.; Park, G. G.; Joo, S. H. *Angew. Chem. Int. Ed.* **2014**, *126*, 4186.
(8) Xu, J.-J.; Xiao, C.-H.; Ding, S.-J. *Chinese Chem. Lett.* **2017**, *28*, 748.
(9) Wang, J.; Wu, Z.-X.; Han, L.-L.; Liu, Y.-Y.; Guo, J.-P.; Xin, H. L.; Wang, D.-L. *Chinese Chem. Lett.* **2016**, *27*, 597.
(10) Sheng, W.; Gasteiger, H. A.; Shao-Horn, Y. *J. Electrochem. Soc.* **2010**, *157*, B1529.
(11) Schmidt, T.; Ross, P.; Markovic, N. *J. Electroanal. Chem.* **2002**, *524*, 252.
(12) Sheng, W.; Zhuang, Z.; Gao, M.; Zheng, J.; Chen, J. G.; Yan, Y. *Nat. Commun.* **2015**, *6*, 5848.
(13) Durst, J.; Siebel, A.; Simon, C.; Hasché, F.; Herranz, J.; Gasteiger, H. A. *Energy Environ. Sci.* **2014**, *7*, 2255.
(14) Zheng, J.; Sheng, W.; Zhuang, Z.; Xu, B.; Yan, Y. *Sci. Adv.* **2016**, *2*, 1501602.
(15) Wang, Y.; Wang, G.; Li, G.; Huang, B.; Pan, J.; Liu, Q.; Han, J.; Xiao, L.; Lu, J.; Zhuang, L. *Energy Environ. Sci.* **2015**, *8*, 177.
(16) Sheng, W.; Myint, M.; Chen, J. G.; Yan, Y. *Energy & Environ. Sci.* **2013**, *6*, 1509.
(17) Scofield, M. E.; Zhou, Y.; Yue, S.; Wang, L.; Su, D.; Tong, X.; Vukmirovic, M. B.; Adzic, R. R.; Wong, S. S. *ACS Catal.* **2016**, *6*, 3895.
(18) Strmcnik, D.; Uchimura, M.; Wang, C.; Subbaraman, R.; Danilovic, N.; van der Vliet, D.; Paulikas, A. P.; Stamenkovic, V. R.; Markovic, N. M. *Nat. Chem.* **2013**, *5*, 300.
(19) Bolza´n, A. E. *J. Electroanal. Chem.* **1995**, *380*, 127.
(20) Zadick, A.; Dubau, L.; Sergent, N.; Berthomé, G.; Chatenet, M. *ACS Catal.* **2015**, *5*, 4819.
(21) Zhou, H.; Yang, X.; Li, L.; Liu, X.; Huang, Y.; Pan, X.; Wang, A.; Li, J.; Zhang, T. *ACS Catal.* **2016**, *6*, 1054.
(22) Furukawa, S.; Suga, A.; Komatsu, T. *ACS Catal.* **2015**, *5*, 1214.
(23) Sarkar, S.; Jana, R.; Suchitra; Waghmare, U. V.; Kuppan, B.; Sampath, S.; Peter, S. C. *Chem. Mater.* **2015**, *27*, 7459.
(24) Wang, C.; Chen, D. P.; Sang, X.; Unocic, R. R.; Skrabalak, S. E. *ACS Nano* **2016**, *10*, 6345.
(25) Cui, Z.; Chen, H.; Zhao, M.; DiSalvo, F. J. *Nano Lett.* **2016,** *4*, 2560.
(26) Yu, Y.; Sun, K.; Tian, Y.; Li, X. Z.; Kramer, M. J.; Sellmyer, D. J.; Shield, J. E.; Sun, S. *Nano Lett.* **2013**, *13*, 4975.
(27) Cui, Z.; Li, L.; Manthiram, A.; Goodenough, J. B. *J. Am. Chem. Soc.* **2015**, *137*, 7278.
(28) Wang, X.; Choi, S. I.; Roling, L. T.; Luo, M.; Ma, C.; Zhang, L.; Chi, M.; Liu, J.; Xie, Z.; Herron, J. A.; Mavrikakis, M.; Xia, Y. *Nat. Commun.* **2015**, *6*, 7594.
(29) Xiao, W.; Cordeiro, M. A. L.; Gong, M.; Han, L.; Wang, J.; Bian, C.; Zhu, J.; Xin, H. L.; Wang, D. *J. Mater. Chem. A* **2017,** 5, 9867.
(30) Sheng, W.; Bivens, A. P.; Myint, M.; Zhuang, Z.; Forest, R. V.; Fang, Q.; Chen, J. G.; Yan, Y. *Energy Environ. Sci.* **2014**, *7*, 1719.
(31) Lu, S.; Zhuang, Z. *J. Am. Chem. Soc.* **2017,** *139***,** 5156.
(32) Alia, S. M.; Pivovar, B. S.; Yan, Y. *J. Am. Chem. Soc.* **2013**, *135*, 13473.
(33) Wang, D.; Xin, H. L.; Hovden, R.; Wang, H.; Yu, Y.; Muller, D. A.; DiSalvo, F. J.; Abruña, H. D. *Nat. Mater.* **2013**, *12*, 81.
(34) Nilsson, J.; Carlsson, P.-A.; Grönbeck, H.; Skoglundh, M. *Top. Catal.* **2017**, *60*, 283.
(35) Wang, H.; Abruna, H. D. *J. Am. Chem. Soc.* **2017**, *139*, 6807.
(36) Miller, H. A.; Lavacchi, A.; Vizza, F.; Marelli, M.; Di Benedetto, F.; D'Acapito, F.; Paska, Y.; Page, M.; Dekel, D. R. *Angew. Chem. Int. Ed.* **2016**, *55*, 6004.

SYNOPSIS TOC